ADVANCED ELECTRONIC MATERIALS Open Access
www.advelectronicmat.de



# Mapping of Spin-Wave Transport in Thulium Iron Garnet Thin Films Using Diamond Quantum Microscopy

*Rupak Timalsina, Haohan Wang, Bharat Giri, Adam Erickson, Xiaoshan Xu, and Abdelghani Laraoui**

**Spin waves, collective dynamic magnetic excitations, offer crucial insights into magnetic material properties. Rare-earth iron garnets offer an ideal spin-wave (SW) platform with long propagation length, short wavelength, gigahertz frequency, and applicability to magnon spintronic platforms. Of particular interest, thulium iron garnet (TmIG) has attracted huge interest recently due to its successful growth down to a few nanometers, observed topological Hall effect, and spin-orbit torque-induced switching effects. However, there is no direct spatial measurement of its SW properties. This work uses diamond nitrogen-vacancy (NV) magnetometry in combination with SW electrical transmission spectroscopy to study SW transport properties in TmIG thin films. NV magnetometry allows probing spin waves at the sub-micrometer scale, seen by the amplification of the local microwave magnetic field due to the coupling of NV spin qubits with the stray magnetic field produced by the microwave-excited spin waves. By monitoring the NV spin resonances, the SW properties in TmIG thin films are measured as a function of the applied magnetic field, including their amplitude, decay length (≈50 μm), and wavelength (0.8–2 μm). These results pave the way for studying spin qubit-magnon interactions in rare-earth magnetic insulators, relevant to quantum magnonics applications.**

## 1. Introduction

Magnetic insulators are of great interest for spintronics and magnonic platforms due to their low damping, allowing long-distance information transmission without Joule heating.[1] Yttrium iron garnet ($Y_3Fe_5O_{12}$, YIG), is a well-studied ferrimagnetic (FMI) insulator with a long spin-wave coherence length and relatively low damping ($2.3 \times 10^{-4}$), even for nanoscale spin-wave transmission lines.[2] When combined with heavy metals (HMs) like Pt, it exhibits spin transport phenomena such as spin Seebeck,[3] and enables the transport of coherent spin waves due to spin-orbit torque,[4] and spin transfer torque[5] effects within the Pt layer, extending its application to spintronic devices.[1] However, materials with perpendicular magnetic anisotropy (PMA) are desirable for such devices due to their potential for higher magnetic densities. While extensive work has been done on PMA ferromagnetic (FM) metals such as CoFeB,[6] insulators offer advantages over metals.[7] Their PMA originates from bulk resulting in low current densities when interfaced to HMs.[8–10] Rare-earth (RE) iron garnet insulators ($RE_3Fe_5O_{12}$, REIG) possess a complex unit cell with low damping and the dominant super-exchange interactions between magnetic sublattices $Fe^{+3}$ (Tetrahedral, Tet) with $RE^{+3}$ (Dodecahedral, Dod) and $Fe^{+3}$ (Octahedral, Oct) respectively gives rise the FMI behavior.[11,12] By selecting the RE element, the REIG magnetic properties (compensation temperature $T_M$, saturation magnetization $M_S$, magnetic anisotropy $K$, damping $\alpha$) can be tuned. In particular, thulium iron garnets ($Tm_3Fe_5O_{12}$:TmIG, **Figure 1a**) with PMA have garnered significant interest due to the observation of spin-orbit torque-induced switching effects.[13,14] The PMA originates from the combination of negative magnetostriction and in-plane compressive strain due to the lattice mismatch with $Gd_3Ga_5O_{12}$ (GGG) substrate,[13,14] leading to low current densities when interfaced with HMs for spin-orbit torque control. Notably, TmIG is also suggested to host topological spin textures,[8,15] further extending its applicability to high-density magnetic data recording.[16]

TmIG has been successfully grown as a thin film with thicknesses in the range of a few nanometers[17,18] and its magnetic damping constant was determined to be $\approx 10^{-2}$ through frequency-dependent ferromagnetic resonance (FMR) measurements.[19] Recent spin-wave (SW) electrical

R. Timalsina, A. Erickson, A. Laraoui
Department of Mechanical & Materials Engineering
University of Nebraska-Lincoln
900 N 16th St. W342 NH., Lincoln, NE 68588, USA
E-mail: alaraoui2@unl.edu

H. Wang, B. Giri, X. Xu, A. Laraoui
Department of Physics and Astronomy and the Nebraska Center for Materials and Nanoscience
University of Nebraska-Lincoln
855 N 16th St, Lincoln, NE 68588, USA

The ORCID identification number(s) for the author(s) of this article can be found under https://doi.org/10.1002/aelm.202300648



**DOI: 10.1002/aelm.202300648**

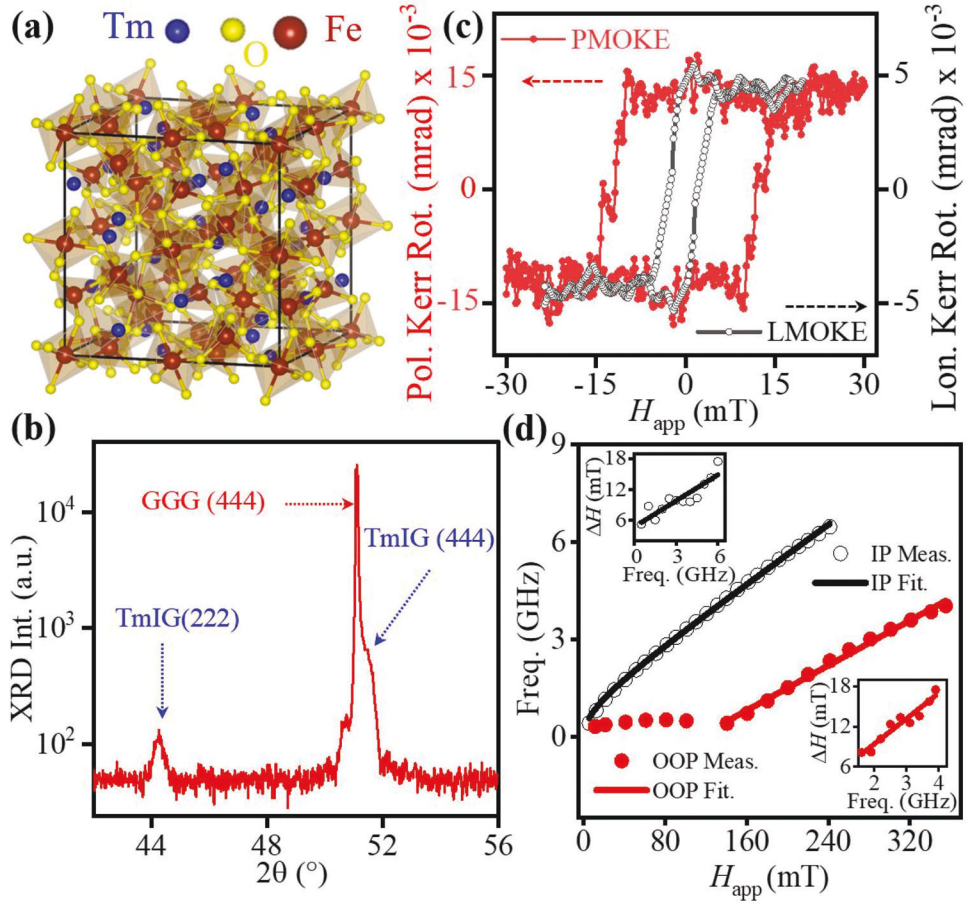


**Figure 1.** a) Crystal Structure of $Tm_3Fe_2(FeO_4)_3$ (TmIG). b) Measured XRD spectrum of 34 nm thick TmIG film grown on 0.5 mm thick GGG substrate showing both TmIG and GGG peaks. c) Polar MOKE (filled-circle-scattered line) and longitudinal MOKE (open-circle-scattered lines) curves versus applied magnetic field of TmIG (34 nm)/GGG. d) In-plane (IP, open circles) and out-of-plane (OOP, filled circles) FMR measurements on TmIG (34 nm)/GGG. Black and red solid lines fit the IP and OOP measurements respectively using the formulas in the main text. Insets of (d) FMR linewidth of IP (open circles) and OOP (filled circles) FMR spectra versus MW frequency. The experimental values are fitted with black and red solid lines for IP and OOP FMR measurements respectively, described in the main text.

transmission studies on undoped[20] and bi-doped[21] TmIG films reported magnetostatic forward volume spin wave modes with a SW group velocity in the range of 0.15–4.9 km $s^{-1}$, and a SW decay length in the range of 3.2–20.5 μm respectively. While these results are promising for using TmIG in magnonic spintronics,[1] there is no direct spatial measurement reported yet of its SW transport properties at the submicron scale.

Various techniques are used to study spatially dependent SW properties in magnetic films and nanostructures such as Brillouin Light Scattering (BLS)[22–24] and magneto-optical Kerr effect (MOKE).[25–27] However, these techniques lack the combined spatial resolution (≈300 nm for BLS and MOKE), experimental flexibility (variable temperatures and magnetic fields), and magnetic sensitivity required to image weakly magnetized materials such as two-dimensional (2D) magnets.[28] An alternative technique has recently emerged for nanoscale measurement of spin waves based on optical detection of the electron spin resonances of nitrogen-vacancy (NV) centers in diamond.[29–33] Negatively charged NVs, composed of substitutional nitrogen adjacent to a vacancy site, are bright and stable emitters that exhibit optically detected magnetic resonance (ODMR) and millisecond spin coherence at ambient conditions,[34] making them an ideal platform to investigate SW properties in REIG magnetic insulators. NV magnetometry has been utilized to probe magnetic dynamic excitations in ferromagnetic thin films and microstructures,[35–38] deduce the chemical potential of the SW bath in YIG,[30] and study the effect of propagating surface SW modes in YIG to amplify externally applied microwave (MW) to excite remote NV locations from the MW source.[29,39] Recently, by using electrically generated spin currents in Pt, an efficient tuning of the YIG magnetic damping was achieved and the amplitude of the magnetic dipole fields generated by a micrometer-sized resonant magnet enabled precise electrical control of the Rabi oscillation frequency of NV spins.[40] Indeed, NV magnetometry offers an enhanced sensitivity at the nanometer scale and has the capability to detect magnons with frequencies up to 100 GHz[41] and with variable wavevectors up to ≈$5 \times 10^7$ $m^{-1}$.[42]

In this work, we use NV magnetometry in combination with SW electrical transmission spectroscopy to study the properties (amplitude, group velocity, wavelength, and decay length)

 

of microwave-excited spin waves in 34 nm thick TmIG films grown on GGG substrates. We measure spatially resolved maps of the stray magnetic field produced by the microwave excited spin waves as a function of the amplitude of the applied magnetic field and find a SW wavelength of 0.8–2 μm, SW decay in ≈50 μm, much longer than earlier studies,[20,21] opening new opportunities of using TmIG in magnonic spintronics[1] and quantum magnonics.[43,44]

## 2. System, Fabrication, and Characterization

### 2.1. TmIG Thin Film Growth and Characterization

We used a pulsed laser deposition (PLD) to grow TmIG thin films (thickness of 34 ± 1 nm) on (111) GGG substrate, closely monitoring using in situ reflection high energy electron diffraction (RHEED), Figure S1a (Supporting Information). As shown in Figure 1b, the X-ray diffraction (XRD) spectra and the RHEED pattern (Figure S1a, Supporting Information) indicate an epitaxial growth. The atomic force microscopy (AFM) topography map (Figure S1c, Supporting Information) confirms the smoothness of the grown film with a root mean square (RMS) surface roughness value ≈0.25 ± 0.5 nm over a 20 × 20 μm scan. Moreover, the observation of the (222) XRD peaks indicates a lattice distortion of the TmIG films caused by the epitaxial strain, because the (222) diffraction peaks are forbidden for the bulk garnet body center cubic (bcc) crystal structure. The positions of the (222) peaks correspond to a 0.349 nm spacing between the (222) planes, which is smaller than the 0.355 nm bulk value, indicating an in-plane tensile strain. The thickness of the fully strained film (critical thickness) is estimated as 5 nm from the width of the (222) peak, while the rest of the film is relaxed. The (444) TmIG diffraction peak is merged with the GGG peak (Figure 1b) and it is clearly seen for a similar thickness TmIG film grown on (111) $Gd_{2.6}Ca_{0.4}Ga_{4.1}Mg_{0.25}Zr_{0.65}O_{12}$ (sGGG), Figure S1b (Supporting Information), explained by the different lattice constants of GGG (1.2382 nm) and sGGG (1.248 nm).[18]

The magnetic properties of the 34 nm thick TmIG/GGG film have been examined using MOKE. As shown in Figure 1c for polar MOKE (PMOKE, filled-circle-scattered line) and longitudinal MOKE (LMOKE, open-circle-scattered line) configurations, near-square-shaped hysteresis loops are observed with coercive field $H_c$ of 2.3 and 11.8 mT for LMOKE and PMOKE respectively. As shown in Figure 1c, the polar Kerr rotation is three times larger than the longitudinal values indicating a slightly out-of-plane (OOP) magnetic anisotropy. We performed vibrating-sample magnetometer (VSM) measurement (Figure S1d, Supporting Information) for in-plane (IP) configuration and found $H_c$ of ≈0.2 mT lower than LMOKE, indicating some of the residual OOP magnetization in the LMOKE loop. The weaker PMA[45] in 34 nm thick TmIG/GGG appears to correlate with the smaller lattice mismatch between TmIG and GGG than that between TmIG and sGGG, where interesting effects such as interfacial Rashba-effect-induced anisotropy were observed.[18]

Ferromagnetic resonance (FMR) spectroscopy is used to measure the magnetic anisotropy, gyromagnetic ratio $\gamma$, and damping constant $\alpha$ values. Figure 1d shows FMR frequency dependence with applied magnetic field $H_{app}$ curves for IP (open circles) and OOP (filled circles) configurations. The IP and OOP FMR resonance frequencies are determined from the derivative of real $S_{11}$ versus $H_{app}$ curves in Figure S3 (see Section S3 Supporting Information). The solid lines in Figure 1dare fits based on the equations of IP and OOP measurements respectively:[18,20,21] $f_{FMR,\ IP} = \mu_0\gamma\sqrt{H_R(H_R + M_{eff})}; f_{FMR,\ OOP} = \mu_0\gamma(H_R + M_{eff})$, $H_R$ is the magnetic field corresponding the FMR resonance, $M_{eff}$ is the effective magnetization $= M_s - H_a$ for IP and $= M_s - H_\perp$ for OOP measurements. $H_a$ is the demagnetizing IP magnetic antitropy, $H_\perp$ is the OOP uniaxial anisotropy.[46] The fitting parameters resulted in $\gamma$ = 22.4 GHz/T, $H_a$= 27 mT, $H_\perp$= 30 mT, and $M_S$ of 66 kA m$^{-1}$. The $M_s$ value agrees well with the VSM measurement shown in Figure S1d (Supporting Information). We also plot the linewidth $\Delta H$ of the FMR IP and OOP measurements (insets of Figure 1d) extracted from the FMR derivative curves in Figure S3 (Supporting Information) as a function of the MW frequency $f$. By fitting the $\Delta H$–$f$ curves with a $\mu_0\Delta H = \mu_0\,\Delta H_0 + \frac{4\pi}{\gamma\alpha f}$ (for IP) $\mu_0\Delta H = \mu_0\,\Delta H_0 + \frac{2\alpha f}{\sqrt{3}\gamma}$ (for OOP), we find a damping value $\alpha$ of 0.0172 for IP measurements and 0.042 for OOP measurements respectively.

### 2.2. Spin-Wave Transmission Spectroscopy of Surface Spin Waves in TmIG Thin Films

For SW transmission spectroscopy, we employ an electrical detection method of spin waves using a vector network analyzer (VNA, Keysight model P5004A).[20,21,47] Ground-signal-ground (GSG) type antennas were fabricated on top of the TmIG film. Refer to Figure 2a, Figure S2a, and Section S2 (Supporting Information) for the nanofabrication details. These antennas are connected to the MW signal probes (Figure S2a, Supporting Information) which are then attached to the VNA using non-magnetic SMA cables. At a given applied MW frequency, a dominating SW mode is excited with a wavevector $k$, determined by the spatial GSG geometry of the stripline (Figure S2a, Supporting Information). We calculate the SW excitation spectra (Figure S2c, Supporting Information) by performing a fast Fourier transform (FFT) of the stray in-plane field $B_y$ generated by the CPW GSG antenna along the $y$ direction (Figure S2b, Supporting Information). The calculated SW modes have wavevector values in the range of $k_1$ = 0.2 rad μm$^{-1}$ for the main SW mode to >5 rad μm$^{-1}$ for the higher SW modes. Here, we focus mainly on measuring the propagating surface spin waves,[22,39] for comparison with subsequent NV measurements.

Figure 2b shows the in-plane real $S_{21}$ SW transmission spectral map as a function of $H_{app}$ applied along $x$ (parallel to the CPW). We plot the real $S_{21}$ spectra at two values of $H_{app}$ at 7 mT (Figure 2c) and 15 mT (Figure 2d), aligned along the $x$ direction, leading to the excitation of magnetostatic surface spin waves (MSSW). A strong dominating mode just above the FMR frequency is seen with additional SW modes, highlighted by the dashed arrows in Figure 2c,d. The intensity of the higher SW modes is weak in comparison to the main and the second SW modes, with good agreement with the calculated spectrum in Figure S2c (Supporting Information). To obtain the signal strength and phase information of the spin waves, we measured the imaginary part of the $S_{21}$ parameter (Im$S_{21}$) as a function of $H_{app}$. The zoomed spectra are plotted in the insets of Figure 2c,d

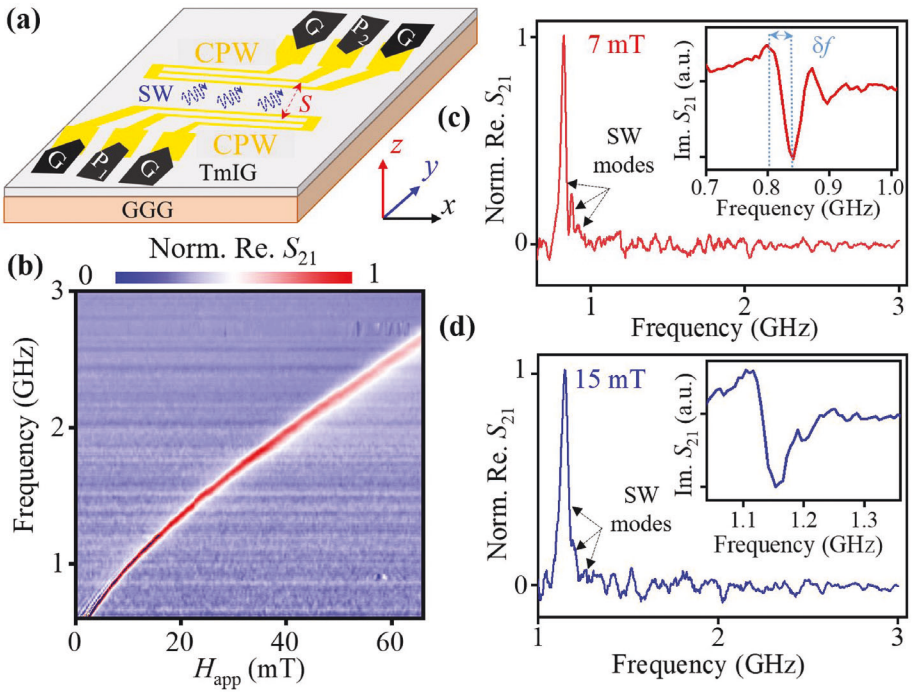


**Figure 2.** a) A schematic of the coplanar waveguides (CPWs) made on TmIG (34 nm)/GGG used for SW electrical transport measurement. b) Normalized real $S_{21}$ intensity of the SW transmission map (MW frequency versus the applied magnetic field $H_{app}$) measured at a MW power of 0.1 mW. Normalized real $S_{21}$ intensity spectral profiles at selected magnetic fields of c) 7 mT and d) 15 mT. Insets: Imaginary $S_{21}$ intensity spectral zoomed profiles measured at the same conditions as in (c) and (d). The SW modes are highlighted by the dashed arrows in (c) and (d).

corresponding to $H_{app}$ values of 7 and 15 mT respectively. We define $\delta f$ as the frequency difference between two adjacent maxima and minima of the Im$S_{21}$ (highlighted in the inset of Figure 2c) corresponding to a SW phase of $\pi$. The SW intensity of the other SW peaks (modes) can be optimized by choosing the distance between the ground and source signal in the CPW to excite them efficiently.[47]

The group velocity ($v_g$) of the spin waves is defined as $v_g = 2\delta f \cdot S$, where $S$ represents the transmission distance of the propagating spin waves (≈32 µm in Figure 2a). We obtained $v_g$ in the range of 0.8–2 km s$^{-1}$. The spin-wave decay length ($l_d$) deduced from the equation $l_d = v_g / 2\pi\alpha f$ falls in the range of 10–30 µm, comparable to CoFe thin films,[48] and higher than the values (≈0.5 µm) obtained in 60 nm thick TmIG films with PMA grown on $Nd_3Ga_5O_{12}$ (NGG) substrates.[20] Spin-wavelength $\lambda$ values in the range of 0.8–2 µm are obtained depending on the magnitude of the applied magnetic field. However, it is quite difficult to obtain the exact values of $\lambda$ and $k$ from electrical measurements that are position-independent.[49] The MW power used for subsequent SW propagation is intentionally kept at 0.1 mW to avoid perturbations in the propagation due to magnetic nonlinearities.[50] To obtain accurate spatial measurements of the SW transport properties in the TmIG/GGG film, we use optically detected magnetic resonance imaging using NV magnetometry (discussed below).

### 2.3. NV Magnetometry

The NV magnetic imaging platform is based on using an electronic grade (100) diamond substrate (2 × 1 × 0.08 mm) doped with a dense (≈1 ppm) NV layer located ≈6–10 nm beneath the surface. The diamond substrate with the NV layer is placed face down on the TmIG film (**Figure 3b**) to probe the interaction of spin waves with NV spin qubits.[31] We detail the diamond substrate and NV creation in Section S4 (Supporting Information). For the experimental setup, we use an optically detected magnetic resonance (ODMR) microscope in the confocal geometry (schematic in Figure 3a) to map surface spin waves in 34 nm thick TmIG/GGG film. A microscope objective (NA = 0.85) is used to focus a 532 nm laser (diffraction spot ≈500 nm) and initialize the NV spin states in $|m_s = 0\rangle$. The resulting NV fluorescence (650–800 nm) is collected by the same objective through a dichroic mirror and detected by a single phone counting module (SPCM). Further details of the experimental setup are described in Section S4 (Supporting Information). The NV spin-triplet ground state (S = 1) exhibits a zero-field splitting $D$ = 2.87 GHz between states $|m_s = 0\rangle$ and $|m_s = \pm1\rangle$.[34] Intersystem crossing to metastable singlet states takes place preferentially for NV centers in the $|m_s = \pm1\rangle$ states, allowing optical readout of the spin state via spin-dependent fluorescence mechanisms.[34] The application of a bias magnetic field $H_{app}$ along the NV symmetry axis (111) breaks the degeneracy of the $|m_s = \pm1\rangle$ state and results in two pairs of spin transitions for NV ensembles whose frequencies depend on the amplitude of magnetic field projection.[51,52] ODMR spectroscopy is implemented by sweeping the MW frequency via a gold (Au) wire (width = 10 µm, length of 200 µm, thickness = 100 nm) fabricated on the TmIG film (Figure 3b), see Section S2 (Supporting Information) for the fabrication details. When the MW frequency is resonant with NV spin transitions, there is a

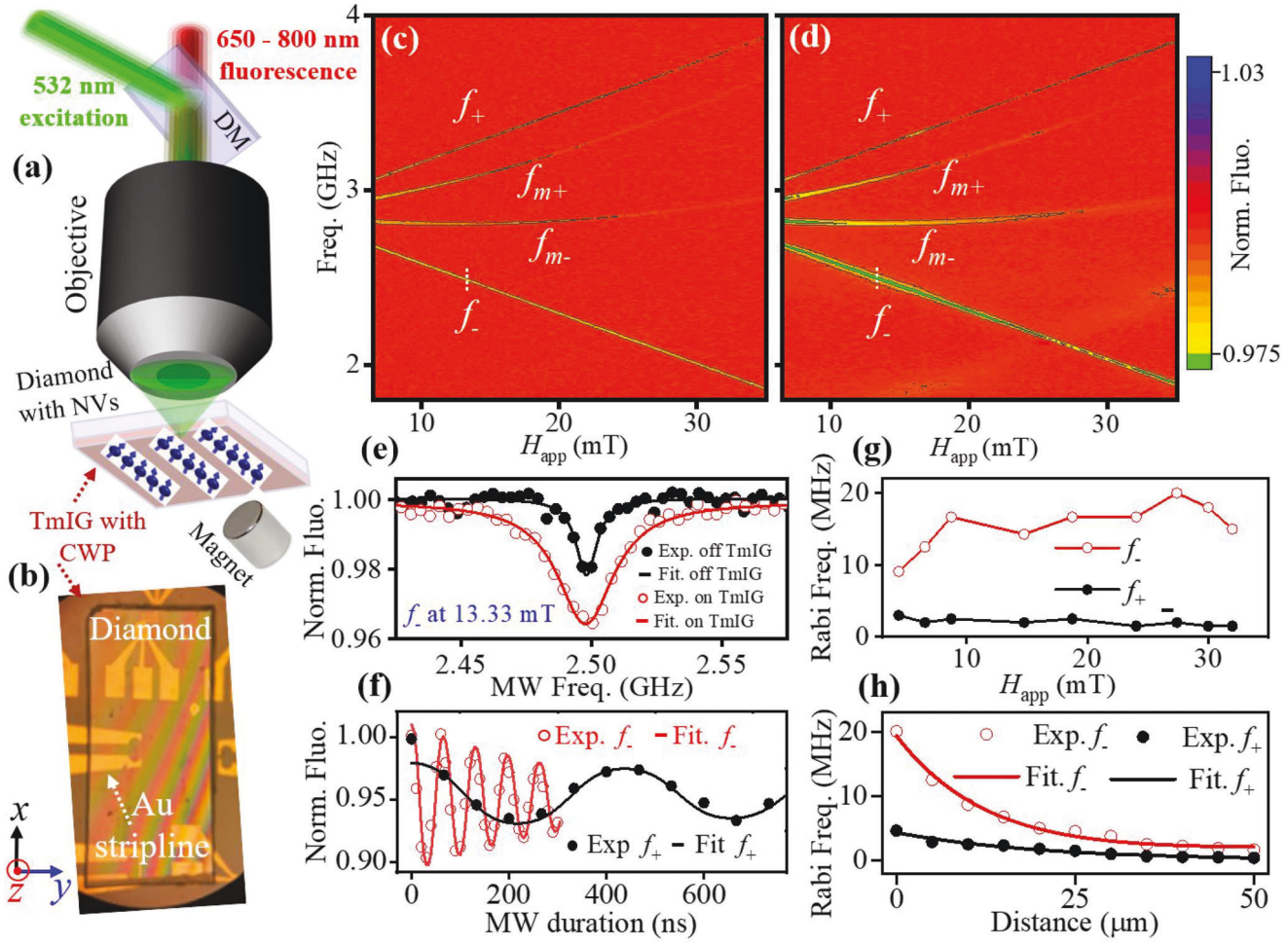


**Figure 3.** a) A schematic of the ODMR microscope in confocal geometry used to map SWs in TmIG/GGG. DM is a dichroic mirror. A green laser (532 nm) initializes the NV center spin and results in fluorescence in the wavelength range of 650–800 nm collected by SPCM. The diamond face with a doped NV layer is in contact with the TmIG film. A permanent magnet is aligned along the [111] axis of the (100) diamond to generate a magnetic field, $H_{app}$, applied with an angle of 35° relative to the TmIG plane. b) A picture of the diamond on top of TmIG with Au striplines to excite SWs for NV and $S_{21}$ measurements. NV ODMR frequency-$H_{app}$ map of diamond on top of Si (off TmIG, c) and (on TmIG d) respectively. e) ODMR $f_-$ signal recorded off TmIG (filled circles) and on TmIG (open circles) at $H_{app}$ = 13.33 mT, highlighted with dashed white lines in (c) and (d) respectively. The black and red solid lines are fitted with the Lorentzian function for off-TmIG and on-TmIG measurements respectively. A clear enhancement of ODMR contrast and linewidth is observed in the SW region of TmIG. f) Rabi oscillations of $f_-$ peak (open circles) and $f_+$ (filled circles) recorded at $H_{app}$ = 13.33 mT and on top of the TmIG film. The MW power is 0.3 W. g) Rabi frequency of $f_-$ peak (open circles) and $f_+$ (filled circles) measured as a function of $H_{app}$. h) Rabi frequency of $f_-$ (open circles) and $f_+$ (filled circles) peaks measured at $H_{app}$ = 13.33 mT as a function of the distance from the stripline along the $y$ direction. The solid red (black) lines are the fitted curves for $f_-$ ($f_+$) measurements, see the main text for the fitting details.

decrease in NV fluorescence. This reduction is related to the occurrence of intersystem crossing, which favors transitions to metastable singlet states, particularly in the $|m_s = \pm 1>$ spin states. Four peaks appear in the ODMR map in Figure 3c (on $SiO_2$/Si, no TmIG) performed at a distance of 5 μm from the Au wire at a MW power of 10 mW: $f_-$, $f_+$ for NV ensembles aligned along [111] and $f_{m-}$, $f_{m+}$ for NV ensemble merged and aligned on the opposite direction.[51,52] The bias magnetic field is applied 35° along the TmIG $xy$ plane and parallel to the Au wire, leading to almost in-plane saturation of the TmIG film.[53] In this geometry, Damon–Eshbach spin-waves (DESWs) can be excited with the same MW injected through the Au wire. By tuning the direction and value of the magnetic field along the NV spin transitions one can probe spin waves with different wavelengths (wavevectors) discussed below.

## 3. Results and Discussion

### 3.1. Effects of Spin Waves on NV Spin Properties

To investigate the effect of the propagating surface spin waves on the NV spins, we conducted identical measurements as shown in Figure 3d where we obtained an ODMR map of the NV-doped diamond in contact with the TmIG film (Figure 3b). A clear enhancement of the ODMR intensity of the low-transition frequency ($f_-$, $f_{m-}$, and $f_{m+}$) peaks is seen in Figure 3d, explained by the frequency overlap between the stray microwave magnetic

field generated by the spin waves and the NV spin transitions.[39] Here, specifically, we concentrate on the effect of the MW excited spin waves on the $f_-$ peak corresponding to the NV ensembles aligned along the NV axis ($\theta = 55^0$ with *z-axis*). In Figure 3e we plot the NV ODMR peak intensity for $f_-$ spin transitions, both off the TmIG film (filled circles) and on the TmIG film (open circles), fitted (solid lines) with Lorentzian function. A substantial enhancement of the ODMR contrast from ≈2% off TmIG to ≈4% on TmIG. The ODMR linewidth $\Delta f$ varies from 9.62 MHz off TmIG to 26.57 MHz on TmIG respectively. These observations are attributed to the resonant energy exchange between the NVs and the propagating spin waves in the TmIG film.[31,54] Particularly, no effect is observed for the $f_+$ peaks at lower magnetic fields, e.g., at 13.33 mT, explained by the lack of frequency overlap between the SW band and NVs spin transitions.[39] The SW amplitude can be deduced from NV magnetometry by measuring the MW magnetic field generated by the propagating spin waves as:[31]

$$B_{SW} = -B^0_{SW} Re\left[\left(\hat{y} + isgn\left(k_y\right)\hat{z}\right) e^{i(k_y y - ft/2\pi}\right] \quad (1)$$

$B^0_{SW} = \mu_0 \ m^0_\perp (1 + sgn(k_y)\eta)|\mathbf{k}| t_{TmIG} e^{-|k_y| d_{NV}}/2$, where $k_y$ is the wavevector of spin waves propagating along $y$ direction, $f$ is the SW frequency, $m^0_\perp$ is the transverse magnetization corresponding to the magnetic stray field of the spin waves traveling perpendicularly to the static magnetization of the TmIG film (Figure 3a), $\eta$ is the SW ellipticity, $d_{NV}$ is the NV-TmIG distance.

To measure accurately the MW magnetic field amplitude generated by the propagating spin waves we use Rabi spectroscopy[55] of NV spins in the proximity of the TmIG film. The NV Rabi frequency $\omega_{Rabi}$ can be retrieved by interfering with the spin wave stray field with a reference MW field $B_{1,Ref}$ as[31]:

$$\omega_{Rabi}\ (y) = \sqrt{2}\ \gamma_{NV} \left| B^0_{SW} \cos^2(\phi/2)\, e^{ik_y y} - B_{1,Ref} \right| \quad (2)$$

where $\gamma_{NV}$ is the NV electron spin gyromagnetic ratio (28 GHz/T), $\phi$ (≈35°) is the angle between the TmIG film plane ($x$, $y$) and the NV axis. Figure 3f displays the Rabi oscillation curves of $f_-$ (open circles) and $f_+$ (filled circles) at $H_{app}$ of 13.33 mT, fitted (solid lines) with a function $\sin(\omega_{Rabi}\, t)\ \exp(-t/T_{1,Rabi})$, $t$ is the MW duration. $T_{1,Rabi}$ (Rabi decay) is 2.27 µs for $f_-$ and 0.34 µs for $f_+$. The decrease of $T_{1,Rabi}$ of the lower $f_-$ spin transitions is explained by the presence of incoherent spin wave noise induced by the excitation of both microwave and thermal SW modes.[42] $\omega_{Rabi}$ is 2.27 MHz for $f_+$ and 15.38 MHz for $f_-$ spin transitions respectively. The increase of $\omega_{Rabi}$ of $f_-$ is further investigated as a function of $H_{app}$ in the range of 4–32 mT (Figure 3g). Frequencies up to 20 MHz are obtained for $f_-$ in the SW band region near (≈0.5 µm) the Au stripline (Figure 3h). For $f_+$, $\omega_{Rabi}$ is in the range of 1.5–3 MHz with a slight decrease at higher magnetic fields explained by the decrease of the MW transmission at higher frequencies of the MW amplifier used in the experiment (Section S4, Supporting Information). $\omega^{f_+}_{Rabi}$ values correspond well to the MW field induced by the Au stripline $B_{1,Ref}$ at the NVs' location ($y_{NV}$ = 5 µm and $d_{NV}$ = 0.8 µm). The distance $d_{NV}$ of ≈0.8 µm between the NVs and TmIG film is estimated by optical, MW, and $T_1$ spectroscopy measurements (Section S5, Supporting Information). Figure 3h shows Rabi frequency $\omega_{Rabi}$ as function of the distance $y$ from the Au wire for $f_-$ and $f_+$ NV spin transitions at $H_{app}$ of 13.33 mT. $\omega^{f_+}_{Rabi}$ decreases away from the Au wire with a decay of ≈20 µm, explained by the decrease of the $B_{1,Ref}$ field along the $y$ direction (see Figure S5a, Supporting Information). However, there is an amplification of $\omega^{f_-}_{Rabi}$ by one order of magnitude at low distances (<10 µm) that decreases to ≈3 MHz for distances up to 50 µm. $\omega^{f_-}_{Rabi}$ is fitted using Equation (2) including both $B_{1,Ref}$ and $B^0_{SW}$ effects. From the fitting parameters and SW amplitude (Section 3.2.) we get a spin-wave amplitude $m^0_\perp$ of 0.016 $M_S$ and a decay length $l_d$ ≈50 ± 5 µm. To obtain the phase information of the spin waves, we employ ODMR continuous-wave imaging.

### 3.2. NV Imaging of Surface Propagating Spin Waves in TmIG

We image the MW excited surface spin waves in 34 nm thick TmIG film by monitoring the NV $f_-$ ODMR intensity as function of the distance from the Au stripline (inset of **Figure 4a**). We apply microwave ($MW_1$) to excite spin waves (above the FMR mode, Figure S6a , Supporting Information) for different values of $H_{app}$. To enhance the SW phase sensitivity of NV magnetometry we apply another microwave ($MW_2$) at the same MW frequency into a Cu wire (diameter of 25 µm) placed on top (≈100 µm) of the diamond substrate and aligned perpendicularly to the Au wire (Figure 6a). $MW_2$ field interferes with the stray field induced by the propagating spin waves excited by $MW_1$ and leads to a spatial standing-wave pattern of the effective AC magnetic field which can be imaged using NV spins.[31,37,42]

To calibrate the measurements on the TmIG/GGG film, we first imaged spin waves excited in 240 nm thick YIG/GGG film under similar conditions, Figure S6c (Supporting Information). A SW wavelength of ≈10 µm is obtained on YIG, in good agreement with earlier NV measurements.[31] In Figure 4b,c we plot the 2D ($x$–$y$) NV normalized fluorescence intensity $FL/FL_0$ map at a frequency $f$ of 2.714 GHz ($H_{app}$ = 5.57 mT) and 2.474 GHz ($H_{app}$ = 14 mT) respectively. $FL$ ($FL_0$) is the fluorescence intensity with (without) MW excitation. Figure 4d shows the integrated (over ten lines) fluorescence intensity cross sections as a function of $y$ distance in the dashed rectangles in Figure 4b,c. Clear oscillations are observed in the curves in Figure 4d explained by the interference of the propagating spin waves excited by $MW_1$ with the uniform reference MW field ($MW_2$). The curves in Figure 4d are fitted with the Equation S4 (Section S7, Supporting Information) and the period of the oscillations corresponds to the wavelength $\lambda$ of the excited SWs. The FFT of the measured normalized fluorescence-distance curves gives the wavevector $k_y$ value associated with the corresponding SW excitation MW frequency at a given applied magnetic field. We detail the fitting and wavevector extraction in Section S7 (Supporting Information). By plotting the frequency of the excited spin waves as a function of the wavevector $k_y$ one can obtain the measured SW dispersion curve from the NV fluorescence spatial maps, Figure 4e. The measured dispersion curve fits well with DESWs $f$–$k$ dispersion curve using Equation S3 and Section S7 (Supporting Information). We find a good fit by using TmIG parameters ($M_s$ = 66 kA m$^{-1}$, $t_{TmIG}$ = 34 nm). $k_y$ increases from ≈4.5 rad µm$^{-1}$ at $H_{app}$ of 14 mT to ≈7.5 rad µm$^{-1}$ at $H_{app}$ of 5.5 mT.

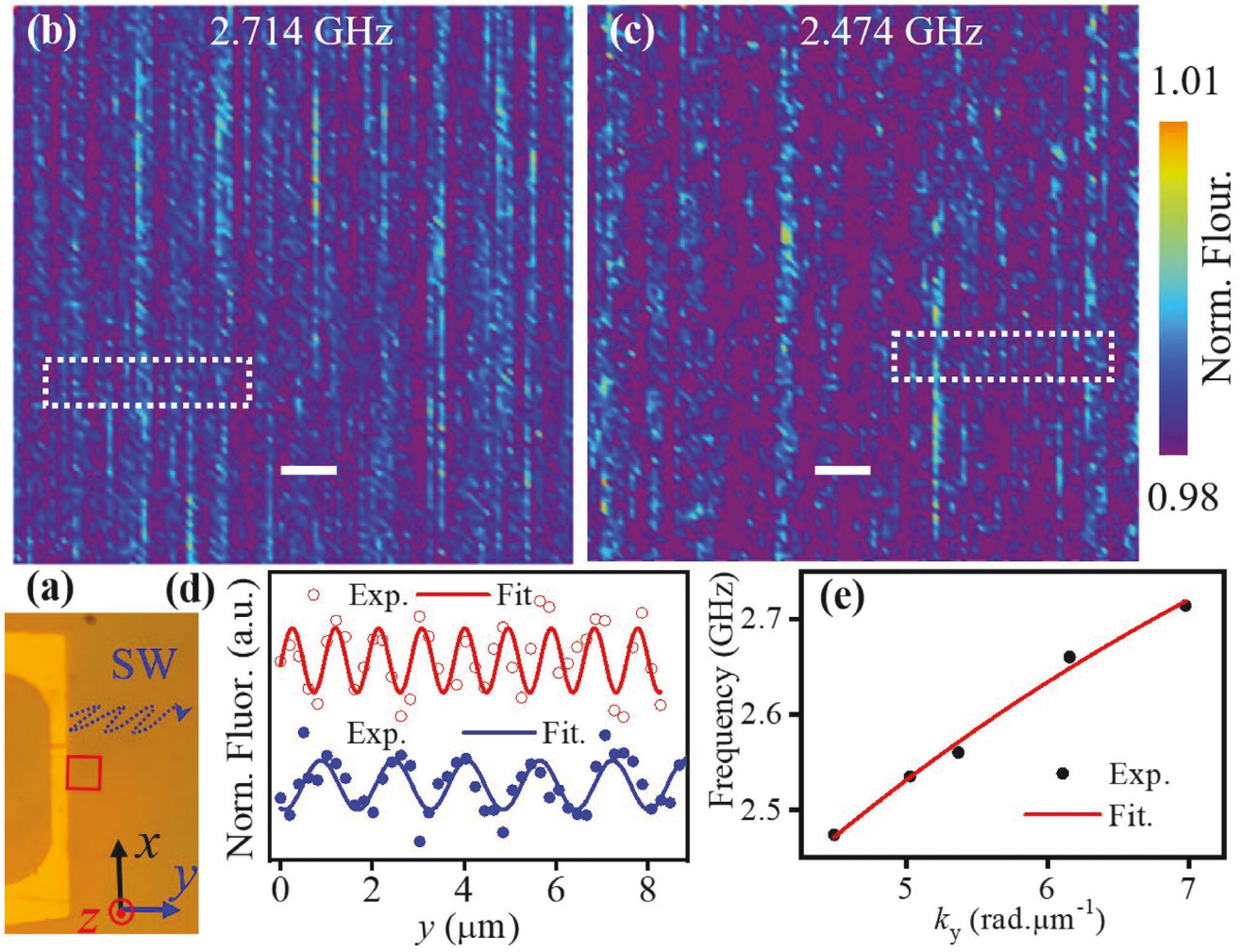


**Figure 4.** NV imaging of surface spin waves in TmIG film. a) a picture of the Au wire made on TmIG in contact with the NV-doped diamond substrate. Spatial maps of the normalized ODMR contrast while driving spin waves in TmIG at $f_-$ of 2.714 GHz at $H_{app}$ = 5.57 mT (b) and $f_-$ of 2.474 GHz at $H_{app}$ = 14 mT (c). The mapped spatial region is highlighted by a solid red square in the inset of (a). $P_{MW}$ = 10 mW and the scale bar in (b) and (c) is 2 μm. The ODMR contrast $FL/FL_0$ is obtained by normalizing the NV fluorescence with MW ($FL$) to that one without MW ($FL_0$) excitation. d) Horizontal cross-sections of the ODMR maps integrated into the dashed rectangles in b (open circles), and c (filled circles), respectively, plotted versus distance $y$ from the Au wire. The solid lines in (d) are fitted using Equation S4 (Supporting Information). e) Measured (filled circles) and calculated (solid line) DESW dispersion curve.

To obtain the SW decay length $l_d$ in the TmIG film, we measure the 2D ($x$, $y$) normalized ODMR contrast map in the area highlighted by the red rectangle in **Figure** 5a (20 × 60 μm). By plotting the integrated normalized ODMR contrast overall $x$ lines in Figure 5b as a function of the distance $y$ from the Au wire, we extract a decay length $l_d$ of 50 ± 5 μm at $H_{app}$ of 12.03 mT (MW frequency is 2.533 GHz, and MW power is 10 mW). The high error in estimating $l_d$ in Figure 5c comes from the spatial variation of the NV density across the diamond substrate,[51,52] that leads to high/low bumps in the NV fluorescence maps (Figure 5b). $l_d$ extracted from NV measurements (≈50 μm) is higher than the value obtained by SW electrical transmission spectroscopy (10–30 μm, Section 2.2.), which may be explained by the different excited SW modes. For example, $k_y$ ≈0.2 rad μm$^{-1}$ for the dominating SW mode is SW transmission spectroscopy measurement (i.e., SWs excited by CPW) and $k_y$ ≈5 rad μm$^{-1}$ for NV measurements (SWs excited by Au wire).

### 3.3. Measuring Interference of Spin Waves in TmIG Thin Film

To investigate spin-wave interference in the TmIG film we measure the 2D ($x$, $y$) NV normalized fluorescence with both $MW_1$ and $MW_2$ applied on resonance with $f$- spin transitions at $H_{app}$ of 10.9 mT (MW frequency is 2.563 GHz and MW power of 10 mW) at the edge of the Au 200 μm long MW wire, **Figure** 6a. At the center of the Au stripline, we observe only one dominant spin-wave mode as in Figures 4 and 5, corresponding to the 1D case.[31] However, when measuring at the edge (inset of Figure 6a) of the stripline we do see an interference pattern as shown in Figure 6b. By performing vertical and transverse cross sections (integrated

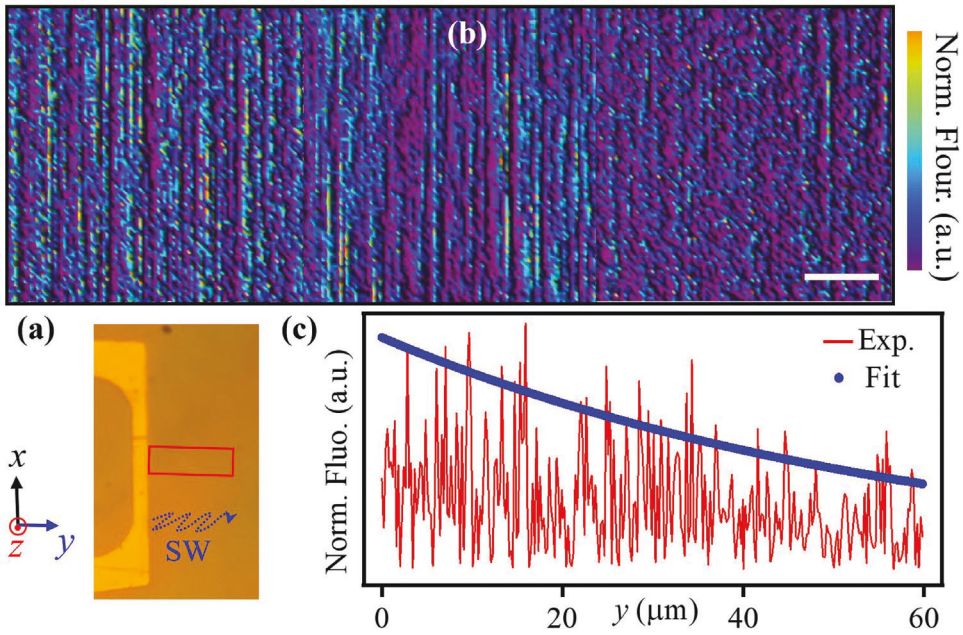


**Figure 5.** NV measurements of spin-wave decay length in 34 nm TmIG film. a) A picture of the Au stripline made on TmIG with the NV scanned area highlighted by the red rectangle. b) Spatial map of the ODMR contrast while driving spin waves in TmIG at $f_-$ of 2.533 GHz at $H_{app}$ = 12.03 mT measured in the highlighted area (red rectangle) in (a). The scale bar in (b) is 5 μm. c) Integrated ODMR contrast over all lines along $x$ as a function of the distance $y$ from the Au wire. The solid line in (c) is a decay fit of the SW amplitude using Equation (1) with a decay of 50 ± 5 μm.

over ten lines in the highlighted dashed lines in Figure 6b) we see interference patterns for the vertical profiles in Figure 6c. The second SW mode is excited by the MW passing through the edge wire (highlighted by a dashed white line) also known as edge effects, leading to obliquely propagating spin waves. The horizontal profiles in Figure 6d show only one SW mode propagating perpendicularly along the MW stripline $k_y$ = 5.37 rad μm$^{-1}$.

Spin-wave interference is observed in 240 nm thick YIG/GGG film when using very weak MW powers,[33] i.e., 500 times less than the MW power used in our experiments. The lower MW power regime prevents broadening and saturating the NV ODMR

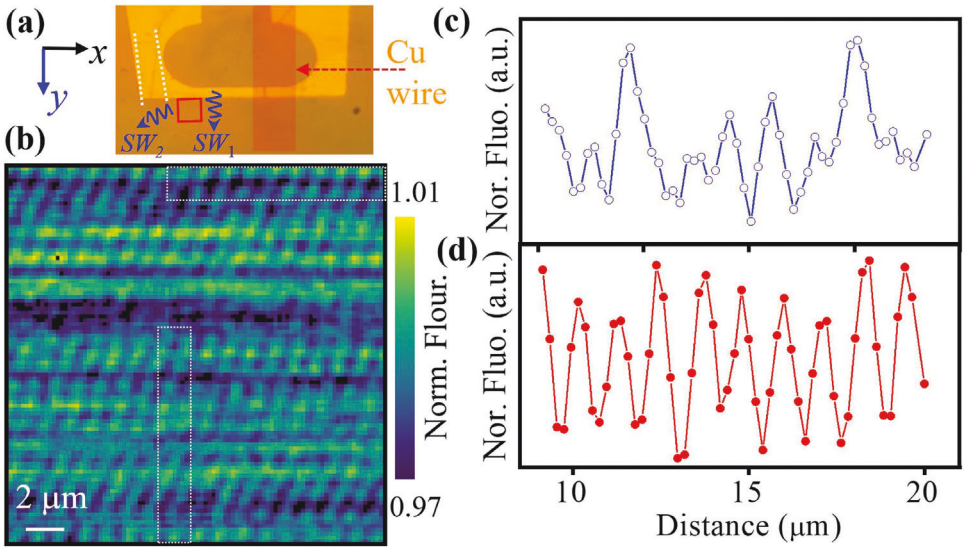


**Figure 6.** NV measurements of spin wave interference in 34 nm TmIG film. a) a picture of the Au stripline configuration on TmIG with diamond doped with NVs facing down. An additional Cu wire perpendicular to the Au stripline is used to induce SW interference with $MW_2$ reference $B_{1,ref}$ field. b) Spatial map of the ODMR contrast while driving spin waves in TmIG at $f_-$ of 2.563 GHz at $H_{app}$ = 10.9 mT measured at the edge of the Au stripline. A clear SW interference is seen in (b) and it comes from the interference between two modes excited with different wavevectors from the center and the edge of the Au stripline. Integrated (over 10 lines) vertical (c, open-circle-scattered line) and horizontal (d, filled-circle-scattered line) cross-sections of the ODMR map in (b) plotted versus distance.

peaks in the presence of spin waves (Figure 3e), and therefore allows imaging of complex rich patterns of spin waves excited in different directions.[33]

## 4. Conclusion

In summary, we use a dense layer of NV spin qubits in diamond to achieve precise phase-sensitive magnetic resonance imaging of coherent surface spin waves in ferrimagnetic insulator TmIG films (thickness of 34 nm) epitaxially grown on GGG substrates. We measure spatially resolved maps of the stray magnetic field produced by the microwave excited spin waves and find a SW wavelength (0.8–2 μm), wavevector values in the range of 4–7 rad $\mu m^{-1}$ that depends on the amplitude of the applied magnetic field and fits well with the dispersion curve of Damon–Eshbach surface spin waves. The spin waves last for distances up to 80 μm with a decay length $l_d \approx 50 \pm 5$ μm, much larger than the values found in earlier studies,[20,21] opening new applications using TmIG in magnonic spintronics[1] and quantum magnonics.[43,44] By engineering the microwave striplines we observe a spin-wave interference between two single-mode SW modes excited by the microwave injected into the central and edge sides of the Au stripline. Studying the engineered spin-wave pattern may reveal an interesting physics of magnon interaction in ferrimagnetic insulators with PMA.[13,14]

This marks the first observation of propagating surface spin waves in TmIG thin films with low saturation magnetization ($M_s$ = 66 kA $m^{-1}$) as compared to YIG ($M_s$ = 142 kA $m^{-1}$). Our results demonstrate the capability of using NV magnetometry to effectively image spin waves (magnons) in weakly magnetized materials such as van der Waals 2D magnets.[28] Future measurements by using NV-diamond scanning probe microscopy (SPM)[56,57] could push down the spatial resolution from ≈500 nm (confocal geometry) to below 50 nm (SPM) and provide more accuracy in filtering and imaging spin waves in ferrimagnetic insulators.[33] Particularly, TmIG with PMA is suggested to host topological spin textures[8,15] and therefore opens the door for NV magnetometry to study the complex interaction between topological spin textures such as skyrmions and magnons.

## Supporting Information

Supporting Information is available from the Wiley Online Library or from the author.

## Acknowledgements

This material is based upon work supported by the NSF/EPSCoR RII Track-1: Emergent Quantum Materials and Technologies (EQUATE) Award OIA-2044049 and NSF award# 2328822. The research was performed in part in the Nebraska Nanoscale Facility: National Nanotechnology Coordinated Infrastructure and the Nebraska Center for Materials and Nanoscience (and/or NERCF), which are supported by NSF under Award ECCS: 2025298, and the Nebraska Research Initiative. The authors thank K. Ambal for helping in setting up the FMR setup and B. Balasubramanian for initial help in VSM measurements.

## Conflict of Interest

The authors declare no conflict of interest.

## Author Contributions

R.T. performed FMR, SW electrical transmission spectroscopy, and NV measurements; H.W. grew the TmIG/GGG films; H.W. and B.G. performed MOKE measurements; A.E. assisted R.T. in AFM measurements; X.X. and A.L. designed the experiments and supervised the project; A.L. wrote the manuscript with contributions of all authors.

## Data Availability Statement

The data that support the findings of this study are available from the corresponding author upon reasonable request.

## Keywords

magnetometry, nitrogen-vacancy, spin waves, rare-earth garnet, thulium iron garnet

Received: September 20, 2023
Revised: October 22, 2023
Published online: December 10, 2023

[1] A. V. Chumak, V. I. Vasyuchka, A. A. Serga, B. Hillebrands, *Nat. Phys.* **2015**, *11*, 453.
[2] Y. Kajiwara, K. Harii, S. Takahashi, J. Ohe, K. Uchida, M. Mizuguchi, H. Umezawa, H. Kawai, K. Ando, K. Takanashi, S. Maekawa, E. Saitoh, *Nature* **2010**, *464*, 262.
[3] K. Uchida, S. Takahashi, K. Harii, J. Ieda, W. Koshibae, K. Ando, S. Maekawa, E. Saitoh, *Nature* **2008**, *455*, 778.
[4] M. Collet, X. De Milly, O. D'allivy Kelly, V. V. Naletov, R. Bernard, P. Bortolotti, J. Ben Youssef, V. E. Demidov, S. O. Demokritov, J. L. Prieto, M. Muñoz, V. Cros, A. Anane, G. De Loubens, O. Klein, *Nat. Commun.* **2016**, *7*, 10377.
[5] L. J. Cornelissen, J. Liu, R. A. Duine, J. B. Youssef, B. J. Van Wees, *Nat. Phys.* **2015**, *11*, 1022.
[6] S. Ikeda, K. Miura, H. Yamamoto, K. Mizunuma, H. D. Gan, M. Endo, S. Kanai, J. Hayakawa, F. Matsukura, H. Ohno, *Nat. Mater.* **2010**, *9*, 721.
[7] A. Hirohata, K. Yamada, Y. Nakatani, I.-L. Prejbeanu, B. Diény, P. Pirro, B. Hillebrands, *J. Magn. Magn. Mater.* **2020**, *509*, 166711.
[8] Q. Shao, Y. Liu, G. Yu, S. K. Kim, X. Che, C. Tang, Q. L. He, Y. Tserkovnyak, J. Shi, K. L. Wang, *Nat. Electron.* **2019**, *2*, 182.
[9] L. Caretta, E. Rosenberg, F. Büttner, T. Fakhrul, P. Gargiani, M. Valvidares, Z. Chen, P. Reddy, D. A. Muller, C. A. Ross, G. S. D. Beach, *Nat. Commun.* **2020**, *11*, 1090.
[10] S. Vélez, J. Schaab, M. S. Wörnle, M. Müller, E. Gradauskaite, P. Welter, C. Gutgsell, C. Nistor, C. L. Degen, M. Trassin, M. Fiebig, P. Gambardella, *Nat. Commun.* **2019**, *10*, 4750.
[11] M. A. Gilleo, S. Geller, *Phys. Rev.* **1958**, *110*, 73.
[12] E. R. Rosenberg, L. Beran, C. O. Avci, C. Zeledon, B. Song, C. Gonzalez-Fuentes, J. Mendil, P. Gambardella, M. Veis, C. Garcia, G. S. D. Beach, C. A. Ross, *Phys. Rev. Mater.* **2018**, *2*, 094405.
[13] C. O. Avci, A. Quindeau, C.-F. Pai, M. Mann, L. Caretta, A. S. Tang, M. C. Onbasli, C. A. Ross, G. S. D. Beach, *Nat. Mater.* **2017**, *16*, 309.
[14] C. O. Avci, E. Rosenberg, M. Baumgartner, L. S. Beran, A. Quindeau, P. Gambardella, C. A. Ross, G. S. D. Beach, *Appl. Phys. Lett.* **2017**, *111*, 072406.
[15] A. S. Ahmed, A. J. Lee, N. Bagués, B. A. Mccullian, A. M. A. Thabt, A. Perrine, P.-K. Wu, J. R. Rowland, M. Randeria, P. C. Hammel, D. W. Mccomb, F. Yang, *Nano Lett.* **2019**, *19*, 5683.
[16] A. Fert, N. Reyren, V. Cros, *Nat. Rev. Mater.* **2017**, *2*, 17031.

[17] A. Quindeau, C. O. Avci, W. Liu, C. Sun, M. Mann, A. S. Tang, M. C. Onbasli, D. Bono, P. M. Voyles, Y. Xu, J. Robinson, G. S. D. Beach, C. A. Ross, *Adv. Electron. Mater.* **2017**, *3*, 1600376.
[18] A. J. Lee, A. S. Ahmed, B. A. Mccullian, S. Guo, M. Zhu, S. Yu, P. M. Woodward, J. Hwang, P. C. Hammel, F. Yang, *Phys. Rev. Lett.* **2020**, *124*, 257202.
[19] C. N. Wu, C. C. Tseng, Y. T. Fanchiang, C. K. Cheng, K. Y. Lin, S. L. Yeh, S. R. Yang, C. T. Wu, T. Liu, M. Wu, M. Hong, J. Kwo, *Sci. Rep.* **2018**, *8*, 11087.
[20] L. Sheng, Y. Liu, J. Chen, H. Wang, J. Zhang, M. Chen, J. Ma, C. Liu, S. Tu, C.-W. Nan, H. Yu, *Appl. Phys. Lett.* **2020**, *117*, 232407.
[21] J. Xu, D. Zhang, Y. Zhang, Z. Zhong, H. Zhang, X. Xu, X. Luo, Q. Yang, B. Liu, L. Jin, *AIP Adv.* **2022**, *12*, 065026.
[22] H. Schultheiss, X. Janssens, M. Van Kampen, F. Ciubotaru, S. J. Hermsdoerfer, B. Obry, A. Laraoui, A. A. Serga, L. Lagae, A. N. Slavin, B. Leven, B. Hillebrands, *Phys. Rev. Lett.* **2009**, *103*, 157202.
[23] M. B. Jungfleisch, W. Zhang, W. Jiang, H. Chang, J. Sklenar, S. M. Wu, J. E. Pearson, A. Bhattacharya, J. B. Ketterson, M. Wu, A. Hoffmann, *J. Appl. Phys.* **2015**, *117*, 17D128.
[24] T. Sebastian, K. Schultheiss, B. Obry, B. Hillebrands, H. Schultheiss, *Front. Phys.* **2015**, *3, 1*.
[25] L. H. F. Andrade, A. Laraoui, M. Vomir, D. Muller, J.-P. Stoquert, C. Estournès, E. Beaurepaire, J.-Y. Bigot, *Phys. Rev. Lett.* **2006**, *97*, 127401.
[26] A. Laraoui, J. Vénuat, V. Halté, M. Albrecht, E. Beaurepaire, J.-Y. Bigot, *J. Appl. Phys.* **2007**, *101*, 09C105.
[27] A. Laraoui, V. Halté, M. Vomir, J. Vénuat, M. Albrecht, E. Beaurepaire, J.-Y. Bigot, *Eur. Phys. J. D* **2007**, *43*, 251.
[28] C. Gong, X. Zhang, *Science* **2019**, *363*, eaav4450.
[29] P. Andrich, C. F. De Las Casas, X. Liu, H. L. Bretscher, J. R. Berman, F. J. Heremans, P. F. Nealey, D. D. Awschalom, *NPJ Quantum Inf.* **2017**, *3:*, 28.
[30] C. Du, T. Van Der Sar, T. X. Zhou, P. Upadhyaya, F. Casola, H. Zhang, M. C. Onbasli, C. A. Ross, R. L. Walsworth, Y. Tserkovnyak, A. Yacoby, *Science* **2017**, *357*, 195.
[31] I. Bertelli, J. J. Carmiggelt, T. Yu, B. G. Simon, C. C. Pothoven, G. E. W. Bauer, Y. M. Blanter, J. Aarts, T. Van Der Sar, *Sci. Adv.* **2020**, *6*, eabd3556.
[32] T. Van Der Sar, F. Casola, R. Walsworth, A. Yacoby, *Nat. Commun.* **2015**, *6*, 7886.
[33] B. G. Simon, S. Kurdi, J. J. Carmiggelt, M. Borst, A. J. Katan, T. Van Der Sar, *Nano Lett.* **2022**, *22*, 9198.
[34] M. W. Doherty, N. B. Manson, P. Delaney, F. Jelezko, J. Wrachtrup, L. C. L. Hollenberg, *Phys. Rep.* **2013**, *528*, 1.
[35] C. S. Wolfe, S. A. Manuilov, C. M. Purser, R. Teeling-Smith, C. Dubs, P. C. Hammel, V. P. Bhallamudi, *Appl. Phys. Lett.* **2016**, *108*, 232409.
[36] M. S. Wolf, R. Badea, J. Berezovsky, *Nat. Commun.* **2016**, *7*, 11584.
[37] T. X. Zhou, J. J. Carmiggelt, L. M. Gächter, I. Esterlis, D. Sels, R. J. Stöhr, C. Du, D. Fernandez, J. F. Rodriguez-Nieva, F. Büttner, E. Demler, A. Yacoby, *Proc. Natl. Acad. Sci. USA* **2021**, *118*, e2019473118.
[38] B. A. Mccullian, A. M. Thabt, B. A. Gray, A. L. Melendez, M. S. Wolf, V. L. Safonov, D. V. Pelekhov, V. P. Bhallamudi, M. R. Page, P. C. Hammel, *Nat. Commun.* **2020**, *11*, 5229.
[39] D. Kikuchi, D. Prananto, K. Hayashi, A. Laraoui, N. Mizuochi, M. Hatano, E. Saitoh, Y. Kim, C. A. Meriles, T. An, *Appl. Phys. Express* **2017**, *10*, 103004.
[40] X. Wang, Y. Xiao, C. Liu, E. Lee-Wong, N. J. McLaughlin, H. Wang, M. Wu, H. Wang, E. E. Fullerton, C. R. Du, *NPJ Quantum Inf.* **2020**, *6*, 78.
[41] F. Casola, T. Van Der Sar, A. Yacoby, *Nat. Rev. Mater.* **2018**, *3*, 17088.
[42] E. Lee-Wong, R. Xue, F. Ye, A. Kreisel, T. Van Der Sar, A. Yacoby, C. R. Du, *Nano Lett.* **2020**, *20*, 3284.
[43] D. D. Awschalom, C. R. Du, R. He, F. J. Heremans, A. Hoffmann, J. Hou, H. Kurebayashi, Y. Li, L. Liu, V. Novosad, J. Sklenar, S. E. Sullivan, D. Sun, H. Tang, V. Tyberkevych, C. Trevillian, A. W. Tsen, L. R. Weiss, W. Zhang, X. Zhang, L. Zhao, C. W. Zollitsch, *IEEE Trans. Quantum Eng.* **2021**, *2*, 5500836.
[44] D. Lachance-Quirion, Y. Tabuchi, A. Gloppe, K. Usami, Y. Nakamura, *Appl. Phys. Express* **2019**, *12*, 070101.
[45] C. Mellinger, J. Waybright, X. Zhang, C. Schmidt, X. Xu, *Phys. Rev. B* **2020**, *101*, 014413.
[46] S. Crossley, A. Quindeau, A. G. Swartz, E. R. Rosenberg, L. Beran, C. O. Avci, Y. Hikita, C. A. Ross, H. Y. Hwang, *Appl. Phys. Lett.* **2019**, *115*, 172402.
[47] J. Solano, O. Gladii, P. Kuntz, Y. Henry, D. Halley, M. Bailleul, *Phys. Rev. Mater.* **2022**, *6*, 124409.
[48] L. Flacke, L. Liensberger, M. Althammer, H. Huebl, S. Geprägs, K. Schultheiss, A. Buzdakov, T. Hula, H. Schultheiss, E. R. J. Edwards, H. T. Nembach, J. M. Shaw, R. Gross, M. Weiler, *Appl. Phys. Lett.* **2019**, *115*, 122402.
[49] J. H. Kwon, S. S. Mukherjee, P. Deorani, M. Hayashi, H. Yang, *Appl. Phys. A* **2013**, *111*, 369.
[50] V. E. Demidov, S. O. Demokritov, K. Rott, P. Krzysteczko, G. Reiss, *J. Phys. D: Appl. Phys.* **2008**, *41*, 164012.
[51] I. Fescenko, A. Laraoui, J. Smits, N. Mosavian, P. Kehayias, J. Seto, L. Bougas, A. Jarmola, V. M. Acosta, *Phys. Rev. Appl.* **2019**, *11*, 034029.
[52] S. Lamichhane, K. A. McElveen, A. Erickson, I. Fescenko, S. Sun, R. Timalsina, Y. Guo, S.-H. Liou, R. Y. Lai, A. Laraoui, *ACS Nano* **2023**, *17*, 8694.
[53] J. Lim, W. Bang, J. Trossman, D. Amanov, J. B. Ketterson, *AIP Adv.* **2018**, *8*, 056018.
[54] P. Che, K. Baumgaertl, A. Kúkol'ová, C. Dubs, D. Grundler, *Nat. Commun.* **2020**, *11*, 1445.
[55] A. Laraoui, C. A. Meriles, *Phys. Rev. B* **2011**, *84*, 161403.
[56] A. Laraoui, K. Ambal, *Appl. Phys. Lett.* **2022**, *121*, 060502.
[57] A. Erickson, S. Q. Abbas Shah, A. Mahmood, I. Fescenko, R. Timalsina, C. Binek, A. Laraoui, *RSC Adv.* **2023**, *13*, 178.